The physical meaning of stark spectroscopy transients from thin film organic semiconducting devices.

Roderick C. I. MacKenzie,[1,2] Anna Göritz,[3] Steve Greedy,[1] Elizabeth von Hauff,[3] and Jenny Nelson[4,2]

[1)] *Faculty of Engineering, University of Nottingham, Nottingham, NG7 2RD UK*

[2)] *FRIAS,University of Freiburg, Albertstr. 19, 79104 Freiburg, Germany*[a)]

[3)] *Institute of Physics, Hermann-Herder-Str. 3a D-79104, Freiburg, Germany*

[4)] *Department of Physics, Imperial College London, South Kensington Campus, London, SW7 2AZ, UK*

Herein, we propose a model to describe picosecond-nanosecond charge separation and non-geminate recombination in organic semiconductors. The model is used to explain time resolved electroabsorption (EA) measurements performed on diodes made from phenyl-C61-butyric acid methyl ester. We find that the measured shape of the EA transient is due to a combination of microscopic carrier dynamic effects such as carrier trapping, as well as macroscopic effects such as band bending caused by the non-uniform poloron generation profile across the device. We demonstrate, that the initial fast phase of the EA transient is due to hot free carriers being able to move freely within the device, over time these hot free carriers cool and become trapped giving rise to the second sower phase of the transient. We further show that the commonly observed dependence of the EA signal on probe wavelength can be explained in terms of the spatial overlap of electrostatic potential within the device and the optical mode of the probe light. Finally, we discuss the implications of these results for pump-probe experiments on thin organic films.

Keywords: charge separation, PCBM, numerical simulation, electroabsorption

[a)]Electronic mail: roderick.mackenzie@nottingham.ac.uk

I. INTRODUCTION

With in the last 12 years the efficiency of organic photovoltaic (OPV) devices has rapidly increased from 2% in 2001 to above 10% today[1]. However, for OPV devices to find commercial applications, their efficiency must be further increased. Key to further boosting cell efficiency is developing a full understanding of the physical mechanisms governing cell operation. The five key physical mechanisms governing the operation and efficiency of OPV devices are; 1) exciton generation[2]; 2) exciton dissociation[3]; 3) charge separation[4,5]; 4) charge transport[6,7]; and 5) non-geminate charge recombination[8–10]. Steady state transport and non-geminate recombination have received considerable attention[9,11–14] and as a result understanding of these processes has considerably improved. Recently Shockley-Read-Hall (SRH) recombination has been identified as being able to describe non-equilibrium carrier trapping and non-geminate recombination in working organic solar cells[8]. However, the physical description of early time scale (picosecond) charge generation and geminate recombination has received less attention within device models. A typical approach is to invoke a competition between geminate pair recombination and field dependent pair separation[15]. However such an approach is not closely supported by experimental measurements of charge separation.

Recently, the observation of a time resolved Stark shift in the electroabsorption (EA) signal has been used to probe the dynamics of charge carriers within the first few picoseconds after laser excitation within polymer:fullerene blends[16,17] and fullerene[18] devices. In these experiments a short ($\approx 150\ fs$) laser pulse is used to photoexcite excitonic states across the

sample and a high external field of around (1 MVm^{-1}) is applied to force dissociation. In studies of PCBM (Phenyl-C61-butyric acid methyl ester) by Cabanillas-Gonzalez et al. the excitons are seen to dissociate instantaneously into electrons and holes then start drifting towards the contacts[18]. The dipole formed between the electrons and holes drifting towards opposite contacts partially shields the active region from the externally applied field. Due to the change in average internal field within the sample the EA peak at 2.3 eV changes in magnitude[18,19]. This change in electroabsorption can be used to monitor the internal field within the sample and hence the spatial separation of the electrons and holes[20].

In this paper we use a time domain device model to describe the early time Stark response of a PCBM diode[18], we choose to model a PCBM diode rather than a polymer:fullerene blend in order to simplify interpretation of the results and because reliable experimental data exists. The model describes non-geminate recombination and carrier trapping using a mechanism similar to one, which has previously been used to describe the steady state JV curve and slow (micro-second) transient measurements from disordered organic materials[8]. Thus for the first time we demonstrate a model which can describe both the fast carrier dynamics a few picoseconds after generation and the slower (ns-μs) recombination processes which define the JV curve and thus efficiency in organic devices. We then apply this model to understand the time resolved Stark spectroscopy data presented by Cabanillas-Gonzalez et al. The result is a better understanding of EA data from films of organic molecules.

II. EXPERIMENTAL DATA

In pump-probe Stark spectroscopy measurements, the field induced change in transmission is given as

$$\Delta^2 T/T = (\Delta T/T)_F - (\Delta T/T). \tag{1}$$

where $(\Delta T/T)_F$ is the transmitted probe signal under field and $(\Delta T/T)$ is the transmitted probe signal under no field. Figure 1 plots Stark spectroscopy data for a PCBM diode as a function of time at different fields obtained by Cabanillas-Gonzalez et al. The pump laser was applied at time 0 and had an energy of 3.2 eV, power density of 0.35 $mJcm^{-2}$ and pulse length of 180 fs[18]. The solid lines within the picture represent the fit of the model (described in detail later) to the experimental data. The inset of figure 1 plots the maximum of the probe signal before the laser pulse is applied against the applied field. The magnitude of the electroabsorption signal is known to change as the square of the field[18],

$$F(t) = (EA/A)^{\frac{1}{2}}. \tag{2}$$

Using linear regression the constant A was found to be $2.5 \times 10^{-13} au\ m^2/V^2$ (see the inset of figure 1). Equation 2 can be used to transform the transient Stark data after the application of the laser pulse in figure 1 to a value of average internal field. Once the average internal field within the device is known, by treating the separating charge pairs as electric dipoles with in a unit volume, the following expression can be derived to relate change of internal field to electron-hole displacement,

$$r(t) = \frac{\epsilon_0 \epsilon_r (F_0 - F(t))}{qn} \tag{3}$$

, where r is the charge pair separation distance, F_0 is the field before the laser pulse is applied, $F(t)$ is the field intensity at time t, n is the dipole density, ϵ_0 is the permittivity of free space, ϵ_r is the relative permittivity (see the supplementary information for a full derivation) and q is the charge on an electron. The charge carrier separation distance extracted from the Stark data is shown in figure 2 as symbols.

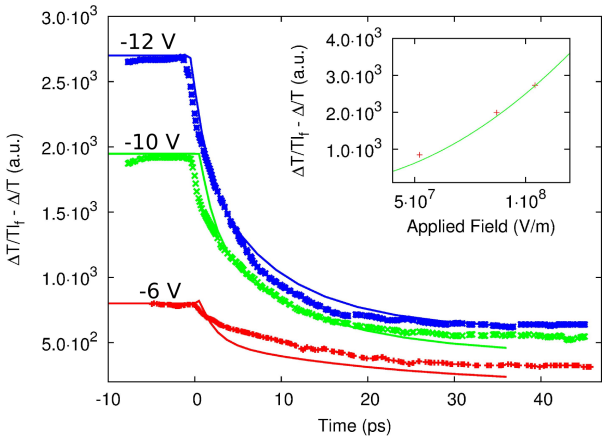

FIG. 1. Evolution of the electroabsorption signal under different applied fields. Simulated (lines) and experimental (points - Cabanillas-Gonzalez's et al.). Inset: Electroabsorption signal v.s field before application of the laser pulse ($t < 0$), the curve is used to transform measured electroabsorption signal to internal electric field.

Once the charge carrier pair separation distance and the field within the device are known, an instantaneous mobility can be defined using

$$\mu = \frac{dr(t)}{dt} / F(t), \tag{4}$$

this is plotted in figure 3 as the lines with points.

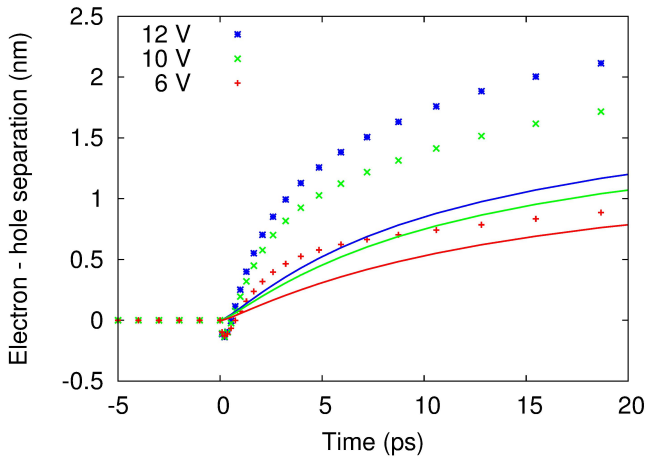

FIG. 2. Charge separation distance extracted from EA data using equation 3 (points). Charge separation data taken directly from numerically calculated carrier profile of the model (lines). The difference between the two data sets is due to equation 3 only considering the microscopic separation of electron hole pairs.

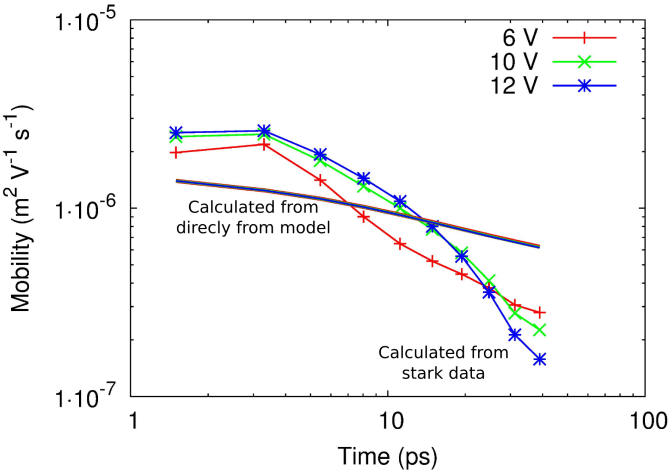

FIG. 3. Instantaneous carrier mobility calculated from the EA data using equation 4 (lines+points), and the instantaneous carrier mobility numerically calculated from the model (lines).

Equation 3 and therefore the above analysis assumes that the measured change in EA signal can be fully described by simply considering the microscopic process of bound pair disassociation. In this interpretation of the experimental results, the microscopic dipole generated by the separating electron and hole shields the medium between them from the externally applied field. This local reduction in field leads to a reduction in the EA signal.

It is assumed that there is a uniform distribution of dipoles throughout the device with density n; that the change in field due to charge separation is also uniform across the device; and that changes to the electric field due to photoexcited carrier dynamics are only a perturbation to the applied field. These assumptions also implicitly assume that carrier generation, recombination, trapping and transport are also uniform across the entire device. However, it is well known from previous studies, that these processes vary strongly as a function of position. For example, the optical generation profile is known to have maxima and minima due to constructive and destructive interference of light within the device[21]. Furthermore, carrier injection and collection at the contacts will create carrier gradients within the device making charge fluxes vary as a function of position. The effect of non uniform generation, injection from electrodes and significant recombination are likely to influence the electric field profile and spatial distribution of excitons, thus influencing the EA response. In the following pages we develop a macroscopic numerical device model to describe carrier separation process across the whole device on the pico-second to nanosecond time scale. We then use this model to obtain a better interpretation of the experimental EA data.

III. NUMERICAL MODEL

The process of excition generation, charge separation, carrier transport, trapping, and recombination must be described in time domain along with the time dependent and electrostatic effects. We use an effective medium approximation to model the fullerene layer[15,22]. To calculate the transient electric field within the diode Poisson's equation is solved,

$$\frac{d}{dx} \cdot \epsilon_0 \epsilon_r \frac{d\phi}{dx} = q(n_f + n_t - p_f - p_t), \tag{5}$$

between the anode ($x = 0$) and cathode ($x = d$), where ϵ_0 is the permittivity of free space, ϵ_r the relative permittivity of the medium, ϕ the (instantaneous) electrostatic potential and q is the electron charge. The transient densities of free electrons, trapped electrons, free holes, and trapped holes are given by n_f, n_t, p_f, p_t respectively. To describe charge transport the drift diffusion equations are solved for positive and negative charge carriers

$$\boldsymbol{J_n} = q\mu_e n_f \frac{\partial E_{LUMO}}{\partial x} + qD_n \frac{\partial n_f}{\partial x}, \tag{6}$$

$$\boldsymbol{J_p} = q\mu_h p_f \frac{\partial E_{HOMO}}{\partial x} - qD_p \frac{\partial p_f}{\partial x}, \tag{7}$$

where J_n and J_p are the electron and hole carrier densities; D_n and D_p are the electron and hole diffusion coefficients; μ_e and μ_h are the carrier mobilities; E_{LUMO} and E_{HOMO} represent the free carrier mobility edges. To force conservation of charges the carrier continuity equations are also solved.

In disordered materials such as those used in organic electronics, it is well known that the presence of localized trap states below the mobility edge[23–27] is a key factor in determining the transport properties[23]. The distribution of energies of such trap states influences the charge dynamics and the relationship between charge density and bias. It has recently been shown that in poly(3-hexylthiophene):phenyl-C61-butyric acid methyl ester (P3HT:PCBM) cells recombination can be described using the Shockley-Read-Hall (SRH)[8,22,28] mechanism in

which carriers recombine when a free charge carrier of one polarity meets a trapped carrier of the other polarity. To account for carrier trap states within our model we introduce exponential distributions of trap states for both electrons

$$\rho^e(E) = N^e exp(E/E_u^e) \tag{8}$$

and holes,

$$\rho^h(E) = N^h exp(E/E_u^h) \tag{9}$$

, where ρ is the energy resolved density of trap states, $N^{e/h}$ is the density of states at the mobility edge and $E_u^{e/h}$ is the characteristic energy of the exponential tails. Although, recent work suggests the trap distribution is more complex than a pure exponential[29], we use an exponential because it has been shown to reproduce experimental data well[22,28–30].

To calculate the spatial photon distribution within the device due to the 3.2 eV pump laser the transfer matrix method[31] is used. This calculates the forward and backward propagating electric fields within the multi-layer device while taking into account interfaces between layers and absorption of the materials. The complex refractive index values for ITO, PEDOT, PCBM and Au are taken from previously published data[32,33].

The full blue line in figure 4 plots the calculated modal profile of the pump light. It is assumed that every absorbed photon generates an electron-hole pair at time $t = 0$. The generation of charge within the model will change the local potential through Poisson's equation (equation 5). By solving Poisson's equation, Coulomb interactions between charges are always included in the model by, so that the electric field charges experience is influenced by

the presence of other charges within the device. Within this picture where all photogenerated charges are included, more and less mobile charges can be distinguished by the gradual relaxation of some of the charges into deeper lying trap states with a consequent reduction in their ability to take part in transport. Those charges that quickly relax into traps could be considered as equivalent to the charge pairs that do not succeed in dissociating within simpler models such as that used by Cabanillas-Gonzalez et al. The local contribution to the EA signal due to the sum of the internal and external fields can be calculated as,

$$I(\omega, t, x) = C\left(\frac{d\phi}{dx}\right)^2 \tag{10}$$

where C is a constant. Therefore, the EA averaged over the entire device is given by

$$\Delta T/T(t, \omega) = d^{-1}\int_0^d I(\omega, t, x)m(x, \omega)dx \tag{11}$$

where $m(x, \omega)$ is the normalized optical modal profile of the *probe* light. As with the pump light, the modal profile of the 2.3 eV probe light within the device over the ITO,PEDOT, PCBM and the gold contact layers, is calculated using a transfer matrix based approach. Thus, in a region of the device where there is constructive interference of the probe light $\Delta T/T(t, \omega)$ is very sensitive to changes in field at that location, however where there is destructive interference of the probe light the measurement is less sensitive to changes in local field at that location. The dashed green line in figure 4 plots the calculated modal profile of the 2.3 eV probe light.

The model was fit to the data in figure 1, the result of the fit is shown as solid lines

plotted with the experimental data (dots). The resulting model parameters are given in the supplementary information. Figure 1 shows that with the given pump and probe wavelengths, the modeled EA signal shows a sharp drop upon excitation then decays more slowly. In the next section we examine carrier distributions within the device as a function of time and visualize the charge separation process.

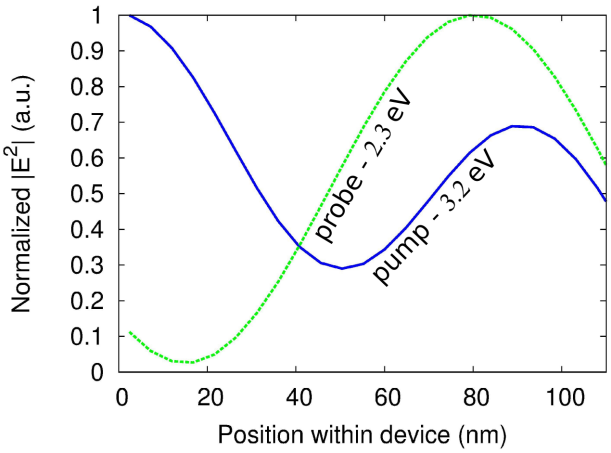

FIG. 4. Calculated photon distributions of light within the solar cell for the pump and probe wavelengths of 3.2 eV and 2.3 eV respectively.

IV. INTERPRETING ELECTROABSORPTION DATA FROM A PCBM DIODE

Figure 5a plots the distribution of carriers within the device just after photoexcitation at 3.2 eV. It can be seen that the initial carrier distribution follows that of the pump photon distribution plotted in figure 4 (blue line). A large negative potential (-6 V) has been applied to the right hand side of the device, therefore as time increases the hole population will drift to the right and the electron population will slide to the left. As these sinusoidal charge carrier distributions pass over one another, dipoles will form where there is a net

positive or negative charge. Such a dipole can be seen in figure 5b at 60 nm, where the net carrier density (hole minus electron) has been plotted at different times. At the right hand side of figure 5b a sharp rise in hole density can be seen. This is due to the photogenerated electron sheet drifting to the left, exposing a net positive charge near the contact. A corresponding but smaller increase in the electron density can be seen on the left hand side of the device. These local changes in charge density, result in local potential changes and thus band bending. This can be seen in figure 5c where the LUMO level (electron mobility edge) has been plotted across the device as a function of time. From figures 5a-c, we can see that the local potential does not reduce uniformly throughout the device as a described by the simple analytical analysis in section II. Instead, the local changes in potential are closely linked to how the initial macroscopic sinusoidal distribution of the photogenerated charge clouds drift/diffuse over each other.

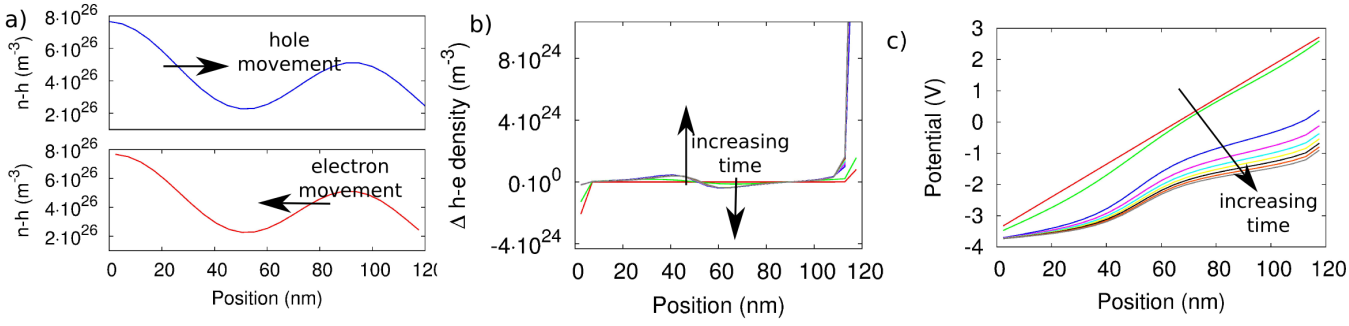

FIG. 5. a) Generation profile of charge carriers within device for a pump energy of 3.2 eV; b) corresponding difference between hole and hole electron populations as a function of time (holes minus electrons) ; and d) resulting bending of the LUMO level within the device.

Sometimes the pump wavelength is varied in an EA experiment[3,34,35] resulting in different shaped EA transients. In the next paragraphs we use the model to theoretically investigate how the chosen pump and probe wavelengths can affect the EA signal. Figure 6a plots the

distribution of photogenerated charge carriers within the device when a pump energy of 2.5 eV is used instead of 3.2 eV. An excitation energy where absorption is weak may be chosen with the aim of generating charges uniformly across a device. The photogenerated carrier distribution at 2.5 eV (figure 6a) is significantly different to that at 3.2 eV (figure 5a). A clear exponential decay can be observed in the distribution at 3.2 eV due to the high absorption of PCBM above 3.1 eV, whereas at 2.5 eV there is no exponential decay in the photon distribution due to the low absorption of PCBM at this energy. The spatial period of the light can also be seen to be longer at 2.5 eV that at 3.2eV.

Figure 6b plots the corresponding net carrier (hole minus electron) density within the device. By comparing figure 6b and figure 5b, it can be seen that, changing the pump energy has shifted the photoinduced charge dipole from 60 nm to the 25 nm and increased its magnitude. The influence this photogenerated charge distribution has on the potential within the device, can be seen in 6c, where the LUMO has again been plotted as a function of time. The LUMO can be seen to bow upwards due to the macroscopic charge dipole centered around 25 nm. The band bending resulting from pumping at 2.5 eV is very different to that observed when the device is pumped at 3.2 eV. Since, the EA signal is proportional to average of the square of the electrostatic field within the device (i.e. how much the bands are bent), we would therefore expect the EA signal from a device pumped at 3.2eV to be very different to a device pumped at 2.5 eV.

The blue line in Figure 7 plots the EA signal corresponding to figures 6a-c. It can be seen that after photoexcitation (at time=0), there is a sudden reduction in EA signal to a minimum at 5 ps, followed by a gradual increase in EA signal between 5 and 40 ps. In

contrast, the corresponding EA response at a pump energy of 3.2 eV in figure 1 (-6 V - red line) shows a gradual reduction in EA signal between 0 and 40 ps. Thus from the above discussion we can say that the choice of pump energy, will determine the initial spatial distribution of photogenerated carriers, which in turn determine where net positive or negative regions of charge within the device are generated and how the bands bend and thus the exact nature of the EA response.

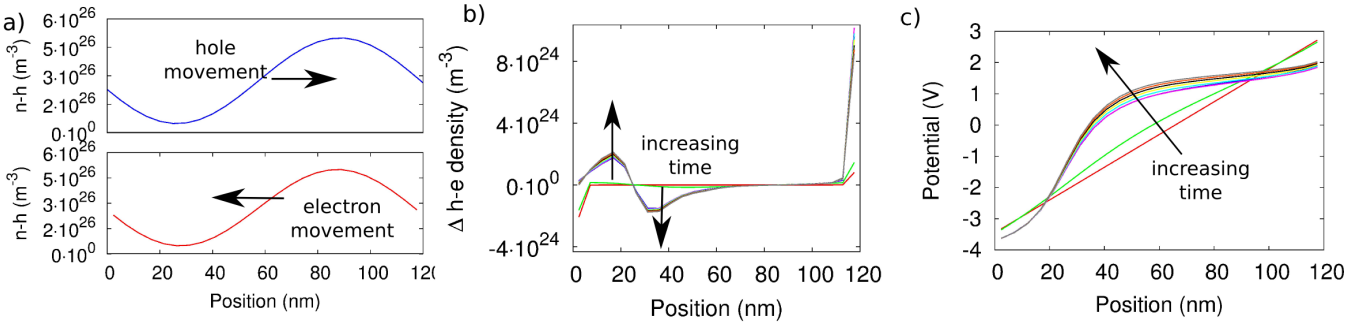

FIG. 6. a) Generation profile of charge carriers within the device for a pump energy of 2.5 eV; b) corresponding difference between hole and hole electron populations as a function of time (hole minus electrons) ; and d) resulting bending of the LUMO level within device. Note, by changing the pump wavelength from 3.2 eV (figure 5) to 2.5 eV, the LUMO band bending is significantly altered. This will also affect the corresponding EA signal.

Not only is the EA signal dependent upon the pump energy, but also upon the chosen probe wavelength. Figure 7 plots the simulated EA responses of the device when probed at 2.6 eV and 3.0 eV (still pumped at 2.5 eV). It can be seen from this figure that not only is the EA signal dependent upon the pump energy, but also upon the chosen probe wavelength. In fact a probe energy of 3.0 eV produces a positive EA response whereas a probe energy of 2.3 eV produces a negative response. This is because the measured EA signal is calculated by multiplying the square of the local electric field by the local photon density of the probe light (equation 11). Thus at a spatial position within the device where the probe light is at a

maximum, the EA signal will be very sensitive to electrostatic potential changes, where the probe light is at a minima, the EA signal will be less sensitive to potential changes. Thus different energies of probe light will sample the non-uniform potential gradients in figure 6c at different places. Figure 8, plots the spatial photon distributions of the 2.3 eV, 2.6 eV and 3.0 eV probe light. It can be seen that the higher the probe energy the more photons there are between in the $0-50nm$ and thus the more sensitive the EA signal will be to the band bending in figure 6c between 0 and $50nm$.

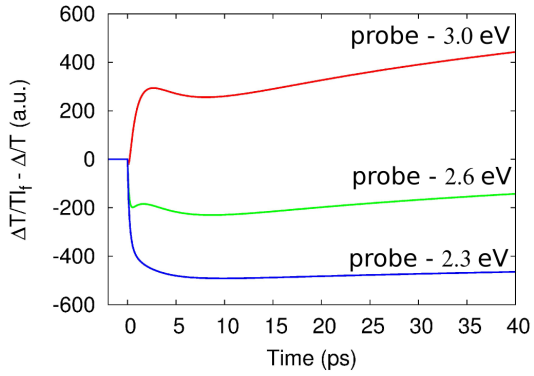

FIG. 7. EA signals for a device pumped at 2.4 eV and probed at 2.3 eV, 2.6 eV and 3.0 eV. It can be seen that by changing the probe energy the EA signal can be significantly altered. This is because different probe energies will have different photon distributions (see figure 8) within the active layer of the device, and thus probe the nonlinear band bending of the device at different spatial locations.

The impact of different light absorption profiles for pump and probe wavelengths is also relevant to time resolved transient absorption measurements which are used to observe the evolution of excited states particularly charge pair generation - on early ($fs-\mu s$) time scales following photoexcitation.[35–39]. Although such experiments are often done on films, where optical interference effects are less pronounced than in devices with reflective back contacts, the effects of different pump and probe wavelengths on the spatial generation of

charges and internal electrostatic fields are still significant. For example, in a recent study of ultrafast transient absorption in blend films of poly[2,1,3-benzothiadiazole-4,7-diyl[4,4-bis(2-ethylhexyl)-4H-cyclopenta[2,1-b:3,4-b]dithiophene-2,6-diyl]:Phenyl-C61-butyric acid methyl ester (PCPDTBT:PC61BM)[3] the authors interpret transient absorption phenomena to the kinetics of exciton dissociation, charge carrier generation and relaxation and stimulated emission, without considering any spatial variation in charge and exciton densities. They attribute changes in dynamics resulting from changes in pump photon energy solely to microscopic phenomena. However, the method we present above would predict a significant influence on the transient absorption as a result of the different pump (1.7-2.4 eV) and probe (0.8-1.5 eV) energies on the macroscopic response of charges in those experiments. Based on the above analysis, we would expect both microscopic carrier relaxation effects and the macroscopic effects to have influenced the recorded transient absorption signal in their measurements.

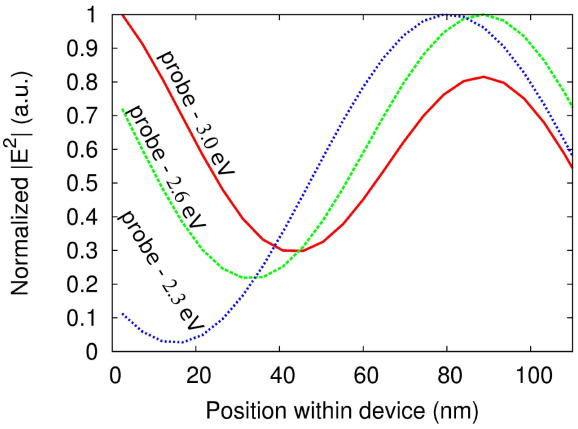

FIG. 8. Normalized modal profiles of the probe light for photon energies of 2.3 (blue), 2.6 (green), and 3.0 eV (red). It can be seen that as photon energy is increased the photon density on the left hand side of the device increases. Thus at low photon energies the EA measurement will only be sensitive to band bending on the right hand side of the device, and while at higher photon energies, the EA measurement will be able to measure average band bending over the whole device.

V. DISCUSSION

Above, we demonstrated that due to constructive and destructive interference the pump light will generate a spatial variation in the internal field electromagnetic of the device. These macroscopic effects were not taken into account in the derivation of the transient charge separation distance (equation 3). Thus, next we examine the validity of equation 3, by comparing the predicted carrier separation distance $r(t)$ to that calculated directly from the carrier populations within the model. Figure 2 plots the charge separation distance calculated directly from Stark data using equation 3. Also plotted in the same figure is the carrier separation distance calculated directly from the modeled internal charge distributions within the model using a geometric average (lines),

$$< x_n >= \frac{\int_0^d (n_f(x) + n_t(x) - n_i) x dx}{\int_0^d n_f(x) + n_t(x) dx}, \tag{12}$$

where n_i is the sum of the initial distributions of trapped and free electrons at the given applied bias, at a time just after the pump laser has generated carriers within the device. An analogous expression can be written for holes. To calculate the average electron-hole separation distance the geometric centers of the charge packets are subtracted $< x >=< x_n > - < x_p >$. If figure 2 is examined, it can be seen that the charge separation distance calculated from the Stark data and the separation of electron and hole centers of mass obtained directly from the model 2 are significantly different. The ultra fast phase seen in the experimental data between $0 - 2$ ps, is far more gradual in the model and the dependence of separation on field is stronger in the experimental data. Furthermore, key to accurately evaluate the

charge separation distance is correctly calculating the the density of photogenerated charge pairs n (equation 3). For the experimental data in figure 2, Cabanillas-Gonzalez et al. estimated the value of $4.6 \times 10^{24} m^{-3}$ by estimating the absorption cross section of the $S_1 - S_n$ states. While, using a transfer matrix model to directly calculate the excition density yields a value of $2.88 \times 10^{26} m^{-3}$. When calculating the curves in figure 2, we used the value of $4.6 \times 10^{24} m^{-3}$ for consistency with Cabanillas-Gonzalez et al.. However, we stress that the total photogenerated excition density also influences the charge dynamics and separation velocity in our model, mainly as a result of the non-uniform electric field in the device.

If figure 2 is examined it can be seen that at early times ($< 10\ ps$) the average charge separation distance increases rapidly, however after this point the charge separation process slows. We can explain this trend by examining what happens to the photo-induced charge within our model as a function of time. Figure 9 plots the time evolution of the density of both free and trapped charge carriers under an applied field of $-6V$. It can be seen that immediately after photo-excitation, free (hot) charge carriers dominate the carrier population then as time passes and the carrier population cools and the number of free charge carriers decreases as the number of trapped carrier increases. Thus there are two distinct regions of the measurement, the first when there are more free carriers than trapped carriers and the other when there are more trapped carriers than free carriers. When carriers are hot and free they can move however once they become trapped movement becomes slow because they must detrap first.

Figure 10(top) plots the calculated charge separation distance extracted directly from the model (using equation 4) as a function of trap density. From the discussion in the

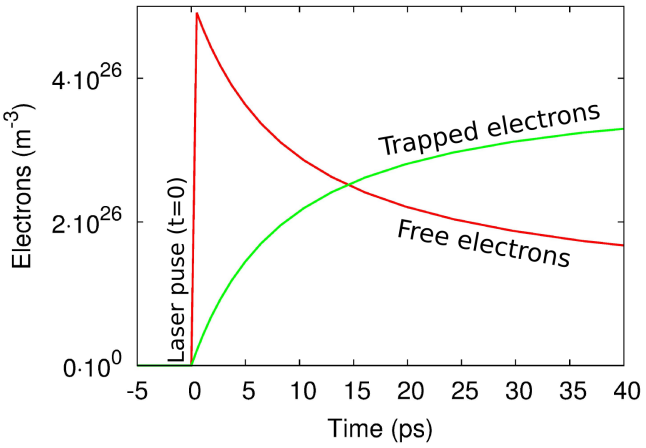

FIG. 9. The average carrier density corresponding to free (hot) and trapped (cool) electrons during the measurement. Initially all photo-generated carriers are free but as they cool they become trapped. It can be seen that during the first 10 ps there are more free carriers than trapped carriers this is the reason for the initial fast separation of the charge packets. It can be seen that past 10 ps most carriers are trapped and thus do not move - this is the reason for the second slow phase to the charge separation transient. At long times the number of trapped carriers decreases this is due to recombination.

previous paragraph, it would be expected that the higher the number of trap states in the material the faster hot carriers would relax into these states and so the slower charge separation would be. This can be seen in figure 10(top) where a larger number of traps slow charge separation. However, when the recombination cross sections are increased (see figure 10(bottom)), the influence of an increased density of trapped states is reversed. This is because more trap states will increase the rate of free-to-trapped carrier recombination, thus increased recombination will change the shape of the carrier clouds over time and so the macroscopic field within the device will also be altered. Therefore, when interpreting EA measurements, it is key to remember that what is being measured is the macroscopic field due to two macroscopic charge clouds moving away from one another rather than a microscopic process, therefore if the shape of the charge clouds changes due to recombination

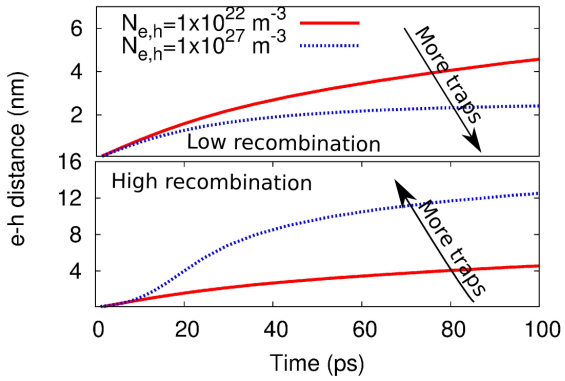

FIG. 10. Influence of trap states on carrier separation distance. When recombination is low the traps act to arrest the separating charge populations. When recombination is high, recombination eats away at the charge packets and causes drift currents and increasing measured separation distance.

or other dynamic events then the estimated microscopic carrier separation distance will also change. We note that recombination is not usually invoked to described fast dynamic effects but intensity dependent recombination has previously been reported on the nanosecond and sub-nanosecond scale[40–42].

Figure 11 plots the average charge separation distance curve at $-6V$ (red line) from figure 2. Also plotted in figure 11 is the average charge separation distance curve for the same simulation where the coulombic electron-hole interaction is turned off by setting the relative permittivity to 1×10^6 (green line); the inset to figure 11 plots the corresponding net charge profile (holes minus electrons) as a function of time. The simulations were carried out with a pump/probe wavelengths identical to those in figure 6a-c. It can be seen that the average charge separation distance increases much more rapidly when the coulombic electron-hole interaction is turned off. If the inset is compared to figure 2b, it can be seen that when there is no electron-hole attraction the net charge profile grows much more quickly as a function of

time, also indicating the electron-hole populations are sliding over each other more quickly. All, this suggests that the coulombic electron-hole attraction is key to determining how fast the electrons and holes can move apart before becoming trapped, and immobile. Indeed if figure 6c is examined there is a flattening of the LUMO centered around $60nm$ which corresponds to the formation of a macroscopic charge dipole around $60nm$ in figure 6b. This flattening of the bands around the dipole is what is responsible for the slow charge separation in figure 11 when coulombic interaction is turned on.

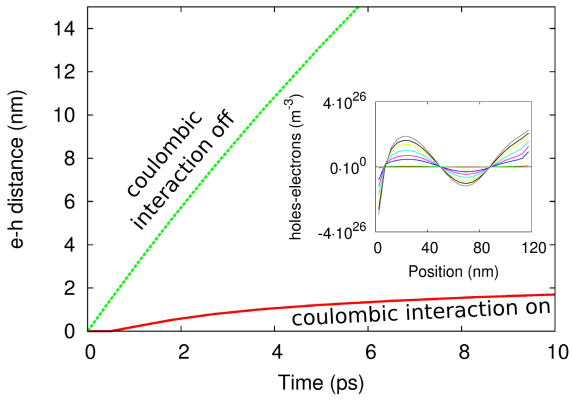

FIG. 11. Simulated charge separation distance with the coulombic effect of charge carriers taken into account (red line), and not taken into account within the simulations (green line). It can be seen that coulombic attraction significantly slows the charge separation process. Inset: The photogenerated electron distribution subtracted from the hole population when coulombic attraction is turned off. It can be seen that when the peaks and troughs of the dipoles are much higher than in figure 5b-6b due to the faster movement of charges.

Cabanillas-Gonzalez et al. also defined a simple equation for calculating instantaneous carrier mobility (equation 4). However, mobility in disordered materials is known to be a strong function of carrier density, this is because the higher the carrier density, the more filled the deep trap states there will be and the are less likely it will be for photogenerated carriers to become trapped. As can be seen from figure 6a, the charge density in the device varies as a strong function of position, thus it is difficult to define a single value of mobility

for the device, so far away from equilibrium. One definition of mobility that has previously been used to define non-equilibrium mobility is

$$\mu_e = \frac{1}{d}\int_0^d \mu_{0e}\frac{n_{free}(x,t)}{nfree(x,t)+n_{trap}(x,t)}dx, \tag{13}$$

where n_{free} is the density of free electrons, n_{trap} the density of trapped carriers, μ_0 the free carrier mobility, x the position within the device and d the thickness. An analogous expression can be defined for the holes.

Both equation 4 and equation 13 have been applied to extract the average carrier mobilities and the results are shown in figure 2. Here, we merely point that out that it is difficult to define a single value of mobility in non-equilibrium situations.

VI. CONCLUSION

We demonstrate that a model including trap states and Shockley-Read-Hall recombination can reproduce experimental charge separation data obtained with sub-picosecond photoinduced Stark spectroscopy under a range of applied fields. We have demonstrated that at least part of the observed time resolved electroabsorption signals is due to dynamic macroscopic charge carrier effects. A non-uniform charge carrier generation profile across the device leads to a non-uniform electrostatic potential profile. Probing at different wavelengths means that potential gradients at different spatial regions are preferentially probed. This varying spatial overlap between the non-uniform internal field and the modal profile of the probe light can significantly influence the measured EA signal. We demonstrate that

macroscopic effects such as non-geminate recombination and band bending can significantly change the effective measured charge separation distance by changing the shape of the charge clouds. The model is able to explain why the measured charge separation distance initially increases rapidly then slows. In our model, the initial fast phase of the transient is due to unrelaxed, or hot charge carriers moving freely within the device. Over time these hot carriers cool and become trapped giving rise to the second phase of the transient. We also discuss the implications of these results for other pump probe experiments. We recommend that different film thicknesss be used to check whether optical interference effects are indeed influencing the measured signal. With the aid of simple optical modeling this strategy could help transient optical and transient electroabsorption measurements to result in a more complete picture of the charge carrier dynamics within the device.

REFERENCES

[1]M. A. Green, K. Emery, Y. Hishikawa, W. Warta, and E. D. Dunlop. *Progress in Photovoltaics: Research and Applications*, 2012, 20 1 12–20.

[2]C. H. Woo, P. M. Beaujuge, T. W. Holcombe, O. P. Lee, and J. M. J. Frchet. *Journal of the American Chemical Society*, 2010, 132 44 15547–15549.

[3]G. Grancini, M. Maiuri, D. Fazzi, A. Petrozza, H. Egelhaaf, D. Brida, G. Cerullo, and G. Lanzani. *Nat Mater*, 2013, 12 1 29–33.

[4]T. M. Clarke and J. R. Durrant. *Chemical Reviews*, 2010, 110 11 6736–6767.

[5]D. Vithanage, A. Deviis, V. Abramaviius, Y. Infahsaeng, D. Abramaviius, R. MacKenzie, P. Keivanidis, A. Yartsev, D. Hertel, J. Nelson, V. Sundstrm, and V. Gulbinas. *Nat*

Commun, 2013, 4.

[6]R. C. I. MacKenzie, J. M. Frost, and J. Nelson. *The Journal of Chemical Physics*, 2010, 132 6 064904.

[7]M. M. Mandoc, F. B. Kooistra, J. C. Hummelen, B. de Boer, and P. W. M. Blom. *Applied Physics Letters*, 2007, 91 26 263505.

[8]R. C. I. MacKenzie, C. G. Shuttle, M. L. Chabinyc, and J. Nelson. *Advanced Energy Materials*, 2012, 2 6 662–669.

[9]M. Hilczer and M. Tachiya. *The Journal of Physical Chemistry C*, 2010, 114 14 6808–6813.

[10]C. L. Braun. *The Journal of Chemical Physics*, 1984, 80 9 4157–4161.

[11]C. Groves and N. C. Greenham. *Phys. Rev. B*, Oct 2008, 78 15 155205.

[12]M. Hilczer and M. Tachiya. *The Journal of Physical Chemistry C*, 2010, 114 14 6808–6813.

[13]L. J. A. Koster, V. D. Mihailetchi, and P. W. M. Blom. *Applied Physics Letters*, 2006, 88 5 052104.

[14]R. A. Street. *Phys. Rev. B*, Aug 2011, 84 7 075208.

[15]L. J. A. Koster, E. C. P. Smits, V. D. Mihailetchi, and P. W. M. Blom. *Phys. Rev. B*, Aug 2005, 72 8 085205.

[16]D. A. Vithanage, A. Deviis, V. Abramaviius, Y. Infahsaeng, D. Abramaviius, J. Nelson, R. C. I. MacKenzie, P. Keivanidis, A. Yartsev, V. Sundstrm, and V. Gulbinas. *Nature Communications*, 2012, 2 6 662–669.

[17]S. Glinas, A. Rao, A. Kumar, S. L. Smith, A. W. Chin, J. Clark, T. S. van der Poll, G. C. Bazan, and R. H. Friend. *Science*, 2014, 343 6170 512–516.

[18]J. Cabanillas-Gonzalez, T. Virgili, A. Gambetta, G. Lanzani, T. D. Anthopoulos, and D. M. de Leeuw. *Phys. Rev. Lett.*, Mar 2006, 96 106601.

[19]V. Gulbinas, R. Kananavičius, L. Valkunas, and H. Bässler. *Phys. Rev. B*, Dec 2002, 66 233203.

[20]J. Cabanillas-Gonzalez, T. Virgili, A. Gambetta, L. Lüer, G. Lanzani, T. D. Anthopoulos, and D. M. de Leeuw. *Phys. Rev. B*, Jan 2007, 75 045207.

[21]R. Hausermann, E. Knapp, M. Moos, N. Reinke, T. Flatz, and B. Ruhstaller. *Journal of Applied Physics*, 2009, 106 10 104507–104507–9.

[22]R. C. I. MacKenzie, T. Kirchartz, G. F. A. Dibb, and J. Nelson. *The Journal of Physical Chemistry C*, 2011, 115 19 9806–9813.

[23]H. Bassler. *Phys. Stat. Sol.(b)*, 1993, 175 15–55.

[24]B. Bohnenbuck, E. von Hauff, J. Parisi, C. Deibel, and V. Dyakonov. *Journal of Applied Physics*, 2006, 99 2 024506.

[25]Y. Roichman and N. Tessler. *Applied Physics Letters*, 2002, 80 11 1948–1950.

[26]F. F. Stelzl and U. Würfel. *Phys. Rev. B*, Aug 2012, 86 075315.

[27]N. Tessler and Y. Roichman. *Organic Electronics*, 2005, 6 56 200 – 210.

[28]T. Kirchartz, B. E. Pieters, J. Kirkpatrick, U. Rau, and J. Nelson. *Phys. Rev. B*, Mar 2011, 83 11 115209.

[29]A. Foertig, J. Rauh, V. Dyakonov, and C. Deibel. *Phys. Rev. B*, Sep 2012, 86 115302.

[30]J. Nelson. *Phys. Rev. B*, Apr 2003, 67 15 155209.

[31]P. Peumans, A. Yakimov, and S. R. Forrest. *Journal of Applied Physics*, 2003, 93 7 3693–3723.

[32]G. F. Burkhard, E. T. Hoke, and M. D. McGehee. *Advanced Materials*, 2010, 22 30 3293–3297.

[33]P. B. Johnson and R. W. Christy. *Phys. Rev. B*, Dec 1972, 6 4370–4379.

[34]J. Cabanillas-Gonzalez, G. Grancini, and G. Lanzani. *Advanced Materials*, 2011, 23 46 5468–5485.

[35]G. Cerullo, S. Stagira, M. Nisoli, S. De Silvestri, G. Lanzani, G. Kranzelbinder, W. Graupner, and G. Leising. *Phys. Rev. B*, May 1998, 57 12806–12811.

[36]A. Devizis, K. Meerholz, D. Hertel, and V. Gulbinas. *Phys. Rev. B*, Oct 2010, 82 155204.

[37]A. Devižis, A. Serbenta, K. Meerholz, D. Hertel, and V. Gulbinas. *Phys. Rev. Lett.*, Jul 2009, 103 027404.

[38]A. Deviis, K. Meerholz, D. Hertel, and V. Gulbinas. *Chemical Physics Letters*, 2010, 498 46 302 – 306.

[39]W. Graupner, G. Cerullo, G. Lanzani, M. Nisoli, E. J. W. List, G. Leising, and S. De Silvestri. *Phys. Rev. Lett.*, Oct 1998, 81 3259–3262.

[40]F. Etzold, I. A. Howard, R. Mauer, M. Meister, T.-D. Kim, K.-S. Lee, N. S. Baek, and F. Laquai. *Journal of the American Chemical Society*, 2011, 133 24 9469–9479.

[41]L. M. Andersson, A. Melianas, Y. Infahasaeng, Z. Tang, A. Yartsev, O. Ingans, and V. Sundstrm. *The Journal of Physical Chemistry Letters*, 2013, 4 12 2069–2072.

[42]F. Etzold, I. A. Howard, N. Forler, D. M. Cho, M. Meister, H. Mangold, J. Shu, M. R. Hansen, K. Mllen, and F. Laquai. *Journal of the American Chemical Society*, 2012, 134 25 10569–10583.

Supplementary information for: The physical meaning of stark spectroscopy transients from thin film organic semiconducting devices.

Roderick C. I. MacKenzie,[1,2] Anna Göritz,[3] Steve Greedy,[1] Elizabeth von Hauff,[3] and Jenny Nelson[4,2]

[1)] *Faculty of Engineering, University of Nottingham, Nottingham, NG7 2RD UK*

[2)] *FRIAS,University of Freiburg, Albertstr. 19, 79104 Freiburg, Germany*[a)]

[3)] *Institute of Physics, Hermann-Herder-Str. 3a D-79104, Freiburg, Germany*

[4)] *Department of Physics, Imperial College London, South Kensington Campus, London, SW7 2AZ, UK*

[a)]Electronic mail: roderick.mackenzie@nottingham.ac.uk

I. PCBM DEVICE FITTING PARAMETERS

To obtain fits to the experimental data, the model parameters were restrained within physically meaningful ranges, the downhill simplex algorithm was then used to vary the model parameters until a good fit to the experimental data was obtained. The density of electron and hole trap states at the mobility edge were allowed to vary between $1 \times 10^{20}\ m^{-3}eV^{-1}$ and $9 \times 10^{27}\ m^{-3}\ eV^{-1}$. The best fit was obtained electron and hole trap densities of $8 \times 10^{27}\ m^{-3}eV^{-1}$ and $1.8 \times 10^{27}\ m^{-3}eV^{-1}$ respectively. When equations 8 and 9 are integrated over energy, the absolute density of trap states $8 \times 10^{26}\ m^{-3}$ and $2 \times 10^{26}\ m^{-3}$ are obtained. Fullerene has a density of around 1×10^{27} molecules per meter cubed, it has a triply degenerate LUMO and a five fold degenerate HOMO. The film in question was deposited by spin casting, consequently the molecules may not be optimally packed; therefore once degeneracy is taken into account trap densities of around $1 \times 10^{26} m^{-3}\ eV^{-1}$ are reasonable.

The free electron and hole moilities of PCBM were allowed to vary between $1 \times 10^{-1}\ m^2V^{-1}s^{-1}$ and $1 \times 10^{-9}\ m^2V^{-1}s^{-1}$, the final values obtained by the model for electrons and holes were $2 \times 10^{-6}\ m^2V^{-1}s^{-1}$ and $7 \times 10^{-7}\ m^2V^{-1}s^{-1}$ respectively. Electron mobility measurements on PCBM obtained by field effect measurements have been reported to give values of[1] $1 \times 10^{-7}\ m^2V^{-1}s^{-1}$, while ToF measurements extrapolated to the zero field conditions have yielded[2] a value of $1 \times 10^{-6}\ m^2V^{-1}s^{-1}$. Hole mobilities have previously been reported at $1 \times 10^{-7}\ m^2V^{-1}s^{-1}$[2]. Thus our values for electron and hole mobilities lye within an order of magnitude of the experimentally reported values.

The *free electron - trapped electron* and the *free hole - trapped hole* capture cross sections (relaxation cross sections) were left unconstrained, the fitting process produced values of $9 \times 10^{-22}\ m^2$ and $9 \times 10^{-20}\ m^2$ respectively. These values are close to previously reported values for material systems containing PCBM of $2.50 \times 10^{-20}\ m^{-2}$ and $4.86 \times 10^{-22}\ m^{-2}$[3,4], and the areas are also smaller than the physical cross section of a C60 molecule which is around $1 \times 10^{-18}\ m^{-2}$.

The *trapped electron - free hole* and the *free electron-trapped hole* capture cross sections (recombination cross sections) were also unrestrained and the fit produced values of $1 \times 10^{-24}\ m^2$ and $1 \times 10^{-25}\ m^2$ respectively. Again, these values are close to those reported for other PCBM containing material systems[3,4]. It should be noted that the recombination cross sections are smaller than the carrier relaxation cross sections. This implies that carrier relaxation is a significantly faster process than recombination, which is physically reasonable as there will be more unoccupied trap sites in the material than occupied trap sites. Thus it will be more probable for a charge carrier to relax to a deeper energetic trap than find a charge carrier of the opposite polarity with which to recombine.

The characteristic energy of the distributions of trap states states was allowed to vary between $150 \times 10^{-3}\ meV$ and $28 \times 10^{-3}\ meV$, the fit produced values of $100.0\ meV$ for both the electrons and holes respectively. For C60 derivatives tail slope energies have been reported as high as $160 - 290\ meV$, while for pure C60 values as low as $48\ meV$ have been reported[5]. The density of electrons and holes at the majority contacts were set to $2 \times 10^{24}\ m^{-3}$ and $8 \times 10^{20}\ m^{-3}$ respectively.

The cell thickness given in the paper of Cabanillas-Gonzalez et al. was $115.0\ nm$, this

value was rounded to the nearest 10 nm and a value of 120 nm used. The thermal velocity of carriers was taken as $1 \times 10^5\ ms^{-14}$. The relative permitivity was taken as 3.9. The LUMO and HOMO mobility edges were taken as $-3.80\ eV$ and $6.10\ eV$ respectively.

II. DERIVATION OF EQUATION 3

The electric displacement field (D) is a function of the electric field (E) and the polarization density (P) of the medium given by

$$D = \epsilon_0 E + P \tag{1}$$

The electric displacement field can be written in terms of the relative permittivity of the medium.

$$E\epsilon_0\epsilon_r = \epsilon_0 E + P \tag{2}$$

A change in the polarization density can be expressed as a change in the electric field by

$$\epsilon_0\epsilon_r(E + \Delta E) = \epsilon_0 E + P + \Delta P \tag{3}$$

Equating the changes in polarization density and field

$$\epsilon_0\epsilon_r \Delta E = \Delta P \tag{4}$$

Polarization density is defined as the average electric dipole moment r per unit volume.

$$\epsilon_0 \epsilon_r \Delta E = qrn \tag{5}$$

giving

$$r = \epsilon_0 \epsilon_r \Delta E / qn \tag{6}$$

III. DETAILED DESCRIPTION OF THE ELECTRICAL MODEL

As described in the main body of the work, the potential distribution within the device is calculated by solving Poisson's equation between the gold back contact and the ITO front contact. The electron and hole current fluxes are calculated by solving the the bi-polar drift diffusion equations. In order to force electron hole conservation we also solve the bi-polar carrier conservation equations.

$$\nabla \cdot \mathbf{J}_n = q \cdot \left(R_n + \frac{\partial n_{free}}{\partial t} \right) \tag{7}$$

$$\nabla \cdot \mathbf{J}_p = -q \cdot \left(R_p + \frac{\partial p_{free}}{\partial t} \right) \tag{8}$$

, where Rn, Rp are the rate at which electrons/holes are removed from the free carrier populations by recombination and carrier trapping. The derivatives on the right hand side of equations 1 and 2 represent the change of free carrier population over time. These equations are derived from a second order moment expansion of the Boltzmann transport equation. A

schematic of the band structure of the model is shown in Figure 1a, where The LUMO and HOMO mobility edges are labeled ELUMO/EHOMO. Using a finite difference scheme the above mentioned equations are solved on a 1D mesh. The mesh is depicted in Figure 1a as black circles, typically 20-30 mesh points are used in the model.

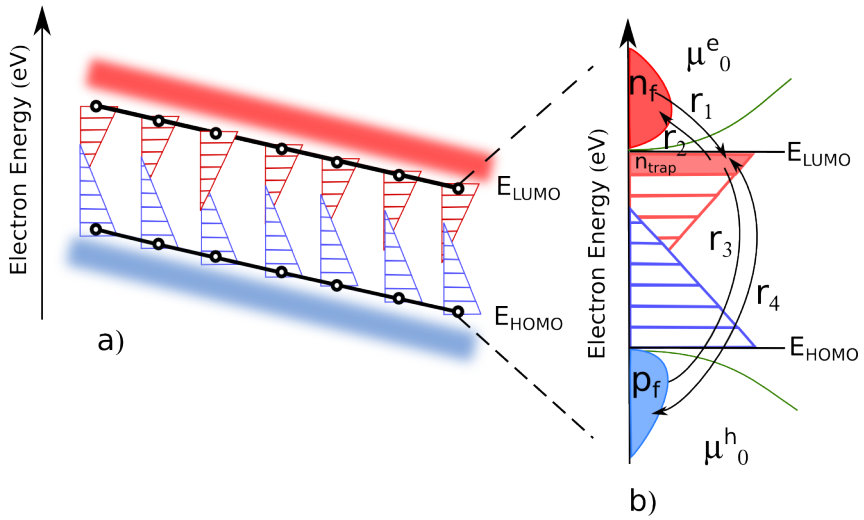

FIG. 1. a) The discretized band structure of the model. The LUMO and HOMO mobility edges are visible as ELUMO and EHOMO, the black circles represent the finite difference mesh points. The red and blue bars represent the free electron/hole carrier distributions. b) A 0D slice down the 1D band structure of the model, the SRH rates are shown along with the free carrier mobilities.

At each mesh point carrier recombination and trapping is accounted for by using the Shockley-Read-Hall (SRH) model, this is depicted in Figure 1b, where a 0D slice down the 1D model in energy space has been depicted. The red and blue filled tear drop shapes represent the free electrons and hole populations respectively within a parabolic band. The trapped electrons and holes are assumed to occupy an exponential distribution of trapped states between ELUMO and EHOMO. The electron and hole exponential distributions are divided into 15 independent trap levels, each with their own independent quasi-Fermi level. The carrier density of each trap level is calculated by evaluating

$$n = \int_{E_{start}}^{E_{stop}} \rho(E) f(E, E_f) dE \tag{9}$$

between Estart and Estop which defines the energetic bounds of the trap state, (E) is the distribution of trap states (see main text), and f is the Fermi-Dirac function

$$f(E, E_f) = \frac{1}{e^{(E-E_f)/kT}} \tag{10}$$

To understand the SRH trapping and recombination mechanism, consider only the capture escape events occurring in the electron trap immediately under the LUMO (filled in with red). There are four rates associated with capture and escape into and out of this trap. Rate r_1 describes carrier capture into the trap from the free electron states, r_2 describes carrier escape from the trap back to the free electron population, r_3 describes the rate at which holes enter the electron trap and rate r_4 the rate at which holes leave the electron trap. The standard SRH rates are given in table I,

Process	label	Rate
electron capture	r_1	$n_f v_{th} \sigma_n N_t (1-f)$
electron escape	r_2	$enNtf$
hole capture	r_3	$pfvthsnNtf$
hole escape	r_4	$epNt(1-f)$

TABLE I. Model parameters used to reproduce the experimental data.

Where vth is the thermal velocity, sn/p are the electron/hole capture cross sections, Nt is the total number of states in the trap. The values en and ep are defined as:

$$e_n = v_{th} \sigma_n N_c exp\left(\frac{E_t - E_c}{kT}\right) \tag{11}$$

and

$$e_n = v_{th}\sigma_p N_v exp\left(\frac{E_v - E_t}{kT}\right) \tag{12}$$

Where Et is the energy of the trap level.

For each electron trap the continuity equation

$$\frac{\partial n}{\partial t} = r_1 - r_2 - r_3 + r_4 \tag{13}$$

is solved. An analogous set of equations can be derived for the hole trap states. This set of capture and escape equations are solve on each mesh point in position space.

Using the above set of equations we are able to describe carrier transport, trapping and recombination in energy and position space across the device. This large set of differential equations is solved simultaneously and self consistently using Newton's method. The drift diffusion equations are discretized using the Scharfetter-Gummel formulation, to account for the exponential dependence of field upon position. The initial guess for the solution is provided by solving Poisson's equation alone and assuming all carrier traps and free/electron populations have the same equilibrium quasi Fermi-level.

Further detail about the model can be found in the papers[3,6].

IV. SOURCE CODE

The source code is available at http://www.organicphotovoltaicdevicemodel.com/.

REFERENCES

[1]E. von Hauff, V. Dyakonov, and J. Parisi. *Solar Energy Materials and Solar Cells*, 2005, 87 14 149 – 156.

[2]S. Tuladhar, D. Poplavskyy, S. Choulis, J. Durrant, D. Bradley, and J. Nelson. *Advanced Functional Materials*, 2005, 15 7 1171–1182.

[3]R. C. I. MacKenzie, C. G. Shuttle, M. L. Chabinyc, and J. Nelson. *Advanced Energy Materials*, 2012, 2 6 662–669.

[4]T. Kirchartz, B. E. Pieters, J. Kirkpatrick, U. Rau, and J. Nelson. *Phys. Rev. B*, Mar 2011, 83 11 115209.

[5]W. ya Zhou, S. shen Xie, S. fa Qian, G. Wang, and L. xi Qian. *J. Phys.: Condens. Matter*, 1996, 8 5793–5800.

[6]F. Deschler, D. Riedel, B. Ecker, E. von Hauff, E. Da Como, and R. C. I. MacKenzie. *Phys. Chem. Chem. Phys.*, 2013, 15 764–769.